PAPER

Check for updates

Synergistically enhanced performance of transition-metal doped Ni$_2$P for supercapacitance and overall water splitting†

Gwaza Eric Ayom, [ID] [a] Malik Dilshad Khan, [ID] [a,b] Jonghyun Choi, [c] Ram Krishna Gupta, [ID] [c] Werner E. van Zyl [ID] [d] and Neerish Revaprasadu [ID] *[a]

Cost-effective and readily available catalysts applicable for electrochemical conversion technologies are highly desired. Herein, we report the synthesis of dithiophosphonate complexes of the type [Ni{S$_2$P(OH)(4-CH$_3$OC$_6$H$_4$)}$_2$] (**1**), [Co{S$_2$P(OC$_4$H$_9$)(4-CH$_3$OC$_6$H$_4$)}$_3$] (**2**) and [Fe{S$_2$P(OH)(4-CH$_3$OC$_6$H$_4$)}$_3$] (**3**) and employed them to prepare Ni$_2$P, Co-Ni$_2$P and Fe-Ni$_2$P nanoparticles. Ni$_2$P was formed by a facile hot injection method by decomposing complex **1** in tri-octylphosphine oxide/tri-*n*-octylphosphine at 300 °C. The prepared Ni$_2$P was doped with Co and Fe employing complexes **2** and **3**, respectively, under similar experimental conditions. Doping Ni$_2$P with Co and Fe demonstrated synergistic improvement of Ni$_2$P performance as an electrocatalyst in supercapcitance, hydrogen evololution and oxygen evolution reactions in alkaline medium. Cobalt doping improved the Ni$_2$P charge storage capacity with a supercapacitance of 864 F g^{-1} at 1 A g^{-1} current density. Fe doped Ni$_2$P recorded the lowest overpotential of 259 mV to achieve a current density of 10 mA cm^{-2} and a Tafel slope of 80 mV dec^{-1} for OER, better than the undoped Ni$_2$P and the benchmark IrO$_2$. Likewise, Fe-doped Ni$_2$P electrode required the lowest overpotential of 68 mV with a Tafel slope of 110 mV dec^{-1} to attain the same current density for HER. All catalysts showed excellent stability in supercapacitance and overall water splitting reactions, indicating their practical use in energy conversion technologies.

Introduction

The current extensive utilization of fossil fuels to generate energy has led to a growing concern for our planet's sustainability. This, in turn, has motivated a quest for zero carbon-based, readily available, and re-usable alternatives to energy generation and storage. Technologies that split water to generate H$_2$ and O$_2$, as well as supercapacitors, hold considerable promise in the area of clean energy generation and storage. The evolution of hydrogen (HER) and oxygen (OER) require suitable catalysts to overcome the uphill energy requirements at the electrodes.[1–3] To date, only noble metals such as Pt, Ru and Ir have been identified as efficient and durable catalysts to

overcome these sluggish reactions. Supercapacitors as energy storage devices are attracting attention due to their excellent power density and cycle life but are restricted by the usage of noble metals as electrodes.[4] The high cost and scarcity of these noble metals therefore constrain the large-scale application of water splitting and supercapacitor technologies.[4,5] Cheaper and readily available alternatives to noble metals are therefore highly sought after.

Nickel phosphides continue to attract attention as catalysts in water splitting and supercapacitance applications.[6–8] The growing attention is due to their abundant earth reserves, high electrical conductivity, fast charge transfer, and good reaction kinetics.[9] Nickel phosphide is a binary system with multiple compositions or phases depending on the ratio of nickel to phosphorus in the system. Its different compositions range from metal-rich phases such as Ni$_2$P, Ni$_{12}$P$_5$, Ni$_3$P, Ni$_7$P$_3$ and Ni$_5$P$_4$ to phosphide rich ones like NiP$_2$ and NiP$_3$.[7,10]

Besides tuning phase, shape and size, doping of different metal atoms into the metal phosphides is another facile and useful strategy employed by researchers to improve the performance of these materials as catalysts for supercapacitors and water splitting.[11] Incorporating a foreign atom in metal phosphides has been illustrated by density functional theory

[a]Department of Chemistry, University of Zululand, Private Bag X1001, KwaDlangezwa 3880, South Africa. E-mail: RevaprasaduN@unizulu.ac.za
[b]Institute of Physical Chemistry, Polish Academy of Sciences, Kasprzaka 44/52, 01-224 Warsaw, Poland
[c]Department of Chemistry, Pittsburg State University, Pittsburg, KS 66762, USA
[d]School of Chemistry and Physics, University of KwaZuluNatal, Westville Campus, Chiltern Hills, Private Bag X54001, Durban, 4000, South Africa

as a route to modifying the adsorption/desorption energies of reactants/products, which is crucial for the activity of a catalyst,[7,12] as well as modulating the density states at the Fermi level and hence improving the reaction kinetics.[13] Moreover, the introduction of another metal in a metal phosphide crystal lattice can cause the redistribution of valence electrons, which in turn provide two electron donation sites leading to improved catalyst performance.[14] For example, Liu *et al.* doped Ni_2P with nitrogen to improve the performance of their electrodes in supercapacitance examinations.[15] Lin *et al.* recently fabricated an iron and oxygen co-doped nickel phosphide that showed good activity in overall water splitting reactions.[16] The performance of nickel phosphide, an excellent catalyst for water splitting[7] can be improved by incorporating Co into its lattice.[13] For example, Qiu *et al.* showed by density functional theory (DFT) analysis that incorporating Co in nickel phosphide leads to an increase in active sites for OH^- adsorption that improves OER activity.[43] Co and Fe-based electrodes have high calculated theoretical supercapacitance values.[17,17,43] The incorporation of a foreign atom into metal phosphides has therefore been demonstrated as a strategy to improve the electronic structure, transfer capability, and density active sites for improved catalytic performance.[11] A survey of the literature, however, shows gaps in doping as a strategy to improve Ni_2P performance (especially Co and Fe) in supercapacitors and water splitting.

Synthesis of phase pure nickel phosphide is challenging due to the existence of nickel phosphide in different compositions. The use of molecular compounds as single-source precursors for the preparation of nanoparticles is well documented.[18] The strengths of this route in nanoparticle preparation over the use of multiple sources lie in the control of ligand design and hence the formation of the suitable metal-phosphide/chalcogenide bonds suitable for the preparation of desired nanomaterials.[5] The exploration of single-source molecular precursors to prepare nickel phosphides is, however, scarce.[7,19] Lukehart and Milne employed a nickel phosphine complex, tetrakis{diphenyl[2-(triethoxysilyl)-ethyl]phosphine} nickel(0), to prepare nickel phosphide nanoclusters in the first report of the use of single-source precursors to make nickel phosphides.[20] Maneeprakorn *et al.* in another study employed dithiophosphinates ([$Ni(Se_2P^iPr_2)_2$], [$Ni(Se_2P^tBu_2)_2$] and [$Ni(Se_2PPh_2)_2$]) as molecular precursors to prepare Ni_2P and Ni_5P_4.[19] Pan *et al.* formed the bis(triphenylphosphine)nickel dichloride complex from the reaction of triphenylphosphine and nickel chloride hexahydrate which was exploited to form nickel phosphides. Habas *et al.* similarly employed triphenylphosphine and a commercially available air-stable nickel phosphine complex [$Ni(PPh_3)_2(CO)_2$] to prepare dinickel phosphide.[21] We also recently demonstrated the solvent-less synthesis of pure phase dinickel phosphide employing dithiophosphonate complexes and triphenylphosphine.[8]

The scarcity of nickel phosphides in the literature particularly formed *via* the single-source precursor route compared to the sulfides or oxides, is attributed to the synthetic difficulties in the formation of desired molecular complexes.

Dithiophosphonate ligands, which are phosphorus and sulfur-containing, are by far the less studied class of the phosphor-1,1-dithiolates. They have rarely been employed to prepare phosphides. Likewise, the preparations of nickel phosphides are constrained by their prolonged reaction time, elevated temperatures[9,22] and the toxicity of reagents usually employed.[23] Furthermore, using precursors with similar structural features for dopants may result in easy and efficient incorporation of dopants, as all the precursors will follow a similar kind of decomposition route.

Herein, we have prepared three dithiophosphonate complexes; [$Ni\{S_2P(OH)(4\text{-}CH_3OC_6H_4)\}_2$] (**1**), [$Co\{S_2P(OC_4H_9)(4\text{-}CH_3OC_6H_4)\}_3$] (**2**) and [$Fe\{S_2P(OH)(4\text{-}CH_3OC_6H_4)\}_3$] (**3**) and explored them as molecular precursors to prepare Ni_2P and Co and Fe-doped Ni_2P with tri-octylphosphine (TOP) as the phosphorus source *via* the hot injection method. The electrocatalytic performance of nickel phosphide and the effect of different concentrations of Co and Fe doping on the performance of the prepared Ni_2P was also investigated for overall water splitting and supercapacitance.

Experimental details

Materials

Tri-octylphosphine (TOP) 90%, trioctylphosphine oxide (TOPO) 90%, nickel chloride hexahydrate, cobalt chloride hexahydrate, iron chloride tetrahydrate, Celite, deionized water, chloroform, acetone, *n*-butanol, phosphorus pentasulfide and anisole were purchased from Sigma Aldrich and used without further purification. Diethyl ether and *n*-hexane were distilled under dinitrogen over a Na wire with the formation of a benzophenone ketyl indicator. Dichloromethane was distilled over P_4O_{10}. Methanol was distilled from I_2/Mg turnings.

Preparation of complexes

The synthesis of complexes **1**, **2** and **3** was carried out according to the established literature procedure.[5] In this procedure, briefly, P_2S_5 was refluxed with excess anisole at 160 °C until all the P_2S_5 dissolved using standard Schlenk techniques. The clear solution was then crystallized on cooling to form 2,4-bis (4-methoxyphenyl)-1,3,2,4-dithiadiphosphetane-2,4-dithione, commonly referred to as Lawesson's reagent (LR). LR was then stirred with stoichiometric amounts of deionized water (**1** and **3**) and *n*-butanol (**2**) until the mixtures went clear. To these clear mixtures were added $NiCl_2 \cdot 6H_2O$, $CoCl_2 \cdot 6H_2O$ and $FeCl_2 \cdot 4H_2O$ to form immediate purple or dark-blue or yellow precipitates which were isolated as complexes **1**, **2** and **3**, respectively.

Complexes **1**, **2** and **3** were confirmed by elemental analysis.

[$Ni\{S_2P(OH)(4\text{-}CH_3OC_6H_4)\}_2$] (**1**): Calc. C: 33.82%; H: 3.24%; S: 25.79%. Found. C: 33.78%; H: 3.30%; S: 25.65%.

[$Co\{S_2P(OC_4H_9)(4\text{-}CH_3OC_6H_4)\}_3$] (**2**): Calc. C: 44.79%; H: 5.47%; S: 21.74%. Found. C: 44.50%; H: 5.42%; S: 21.69%.

[$Fe\{S_2P(OH)(4\text{-}CH_3OC_6H_4)\}_3$] (**3**): C: 44.95%; H: 5.49%; S: 21.81%. Found. C: 45.0%; H: 5.41%; S: 21.79%.

Preparation of Ni$_2$P, Co and Fe doped nanomaterials

Ni$_2$P was prepared from the wet thermolysis of complex **1** following our earlier report.[5] In this procedure, complex **1** (0.20 g, 0.40 mmol) dispersed in TOP (5.0 mL) was quickly injected into TOPO (5.0 g) which had been heated to 300 °C under nitrogen. The black precipitate formed on injection of complex **1** was further heated at 300 °C for 1 hour, cooled to room temperature, washed with methanol/acetone solution, centrifuged and air-dried. 5 and 10% Co and Fe-doped Ni$_2$P were prepared by adding 5 and 10% moles of complexes **2** or **3** to complex **1**, agitating the solid mixtures together and then dispersing them in TOP followed by sonication. The dispersed mixtures were then thermolysed as outlined above.

Instrumentation

The elemental composition of synthesized complexes was obtained on an automated PerkinElmer 2400 series analyzer. Thermogravimetric analyses were performed employing a Mettler-Toledo TGA/DSC at 10 mL min^{-1} flow rate under argon. Powder X-ray diffraction was done *via* a Bruker D8 Discover Diffractometer using CuKα radiation. Scanning electron microscopy (SEM) analyses of particles were carried out using Philips XL30 FEG-SEM. Energy-dispersive X-ray spectroscopy was carried out with a DX4 detector. All analyzed particles were carbon-coated by an Edwards coating system E306A before the SEM analyses. Transmission electron microscopy (TEM) and high-resolution transmission electron microscopy (HRTEM) examinations of the prepared particles were performed employing a JEOL 1400 TEM and JEOL 2100 HRTEM. Materials' preparation for TEM and HRTEM were done by dripping a drop of the diluted particle solution on coated Formvar grids for TEM and holey carbon grids for HRTEM. These prepared particles were left to dry completely at room temperature and then viewed for TEM and HRTEM at voltages of 120 and 200 kV, respectively. Images were acquired images using iTEM software for TEM and Gatan software for HRTEM. The optical properties of particles in dichloromethane were examined by a UV–vis/NIR PerkinElmer Lambda 1050 spectrophotometer. The X-ray photoelectron spectroscopy (XPS) spectra were recorded on a Kratos Axis Ultra DLD spectroscopy. The curve fitting and quantitative analysis was obtained by measuring the area under the elemental and synthesized peaks. Data analysis was conducted using the NIST XPS database for peak assignments.

Electrochemical characterization of the prepared particles was performed using Gamry Potentiostat, which employed a three-electrode system. Sample preparation for electrochemical examinations was done by forming pastes of the particles using the particles (80 wt%), polyvinylidene difluoride (PVDF, 10 wt%), and acetylene black (10 wt%), which was prepared using *N*-methyl pyrrolidinone (NMP) as a solvent. These formed pastes were then applied to pre-cleaned and weighted nickel foams. Dried pastes were then employed as working electrodes. Ni foams (MTI Corporation, USA), 99.99% purity, were used for these investigations. Commercial carbons were

employed as conducting acetylene black (MTI Corporation, USA) with particle sizes ranging between 35–40 nm. Platinum wires and saturated calomel electrodes (SCE) were utilized as counter and reference electrodes, respectively. All the examinations for supercapacitance and electrocatalysis were carried out using 3 M and 1 M KOH electrolyte, respectively. Charge storage capacity was measured using cyclic voltammetry (CV) and galvanostatic charge–discharge (CD) at different scan rates and current densities. Electrocatalytic properties of the prepared electrodes were studied *via* cyclic voltammetry and linear sweep voltammetry (LSV), with LSV done at a scan rate of 2 mV s^{-1} for OER measurements. Electrochemical impedance spectroscopic (EIS) was performed in the frequency range of 0.05 Hz to 10 kHz at an applied AC amplitude of 10 mV.

Results and discussion

Synthetic protocols for the preparation of dithiophosphonate complexes are well reported[5,24,25] and the formation of complexes **1**, **2** and **3** followed these established procedures. The thermal stability and decomposition profile of complexes **1**, **2** and **3** were studied by thermographic analysis (TGA) under inert atmosphere before thermolysis, and the results are shown in the ESI (Fig. S1†). The thermogram of complex **1** indicates multiple-step decomposition, which sets in at 100 °C. The initial decomposition step of complex **1** with 18.9% weight loss correlates to the calculated (21%) loss of the two hydroxyl and methoxy groups of the complex. The decomposition step of complex **1** at 380 °C with 50% weight loss correlates to the calculated (43%) loss of all the organics leaving behind P$_2$S$_4$Ni. According to the TGA, further decomposition of complex **1** leads to phosphorus loss at about 850 °C with only about 19% weight residue left that corresponds to the calculated weight of 18.2% for NiS. TGA of complex **2** shows that it decomposes in 3 steps beginning at 195 °C with an experimental % weight loss of 39. The 39% weight loss of complex **2** indicates the decomposition of all the organics, with only CoS$_6$P$_3$ residue left (calculated residue 40%). The second and third decomposition steps of complex **2** show the further loss of phosphorus and a calculated theoretical % weight residue of 17.1 (Co$_2$S$_3$) that matches well with the experimental value, *i.e.*, 17%. Complex **3** decomposes in a single step, unlike complexes **1** and **2**. Decomposition sets in at 200 °C and ends at 300 °C with an experimental % weight residue of 43% that correlates with the calculated FeP$_2$S$_3$ of 45%. These results indicate that complexes **1–3** are thermally stable and can thermalize cleanly to form metal sulfides or phosphides. We exploited this to form metal phosphides or sulfides from a single molecular precursor in our earlier report.[5]

The hot injection decomposition of complex **1** employing trioctylphosphine oxide (TOPO) as a surfactant and trioctylphosphine (TOP) as a dispersing solvent for 1 hour yielded nickel phosphide, which is consistent with our previous study.[5] The formed nickel phosphide matched well to hexag-
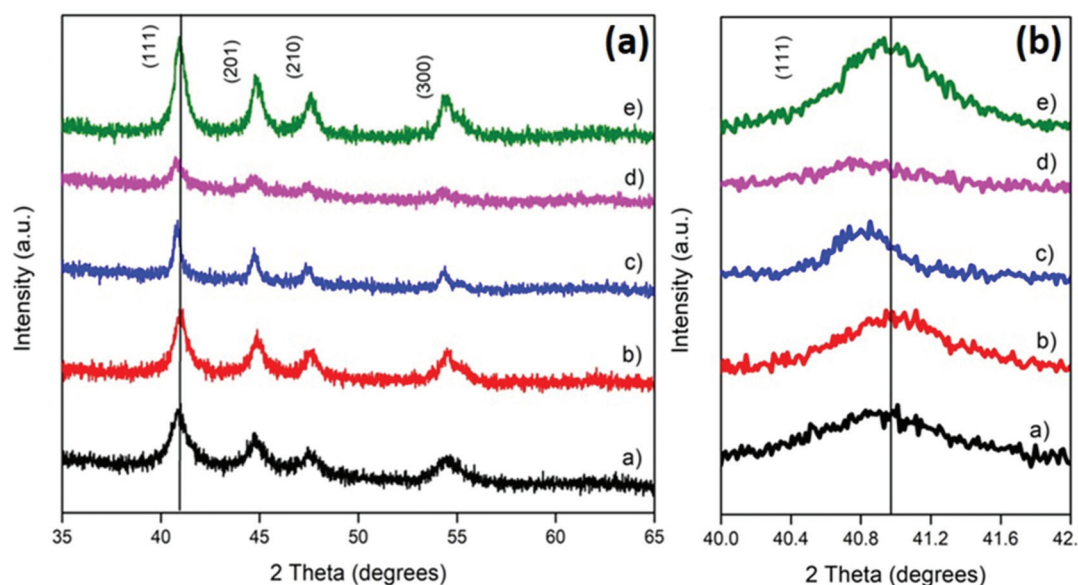
Fig. 1 Diffraction patterns of (a) (a) Ni_2P, (b) 5% Co-doped Ni_2P, (c) 10% Co-doped Ni_2P, (d) 5% Fe-doped Ni_2P and (e) 10% Fe-doped Ni_2P. (b) Magnification of the most intense p-XRD peak of all samples, for comparison.

onal Ni_2P (ICDD# 01-089-2742). It is interesting to note that TOP has been shown to be the phosphorus source in this formation of nickel phosphide despite the presence of intra-molecular phosphorus atoms in complex **1**.[5] Doping Ni_2P with 5 or 10% of complexes **2** (Co) and **3** (Fe) *via* the hot injection route did not change the phase of the nickel phosphide obtained or introduce any impurity. The phase purity of all nanomaterials prepared and the effect of doping was evaluated by p-XRD and is shown in Fig. 1a. The sharp p-XRD diffraction patterns of Ni_2P, Co and Fe-doped Ni_2P are well matched to pure hexagonal Ni_2P and are indexed as per standard reference pattern (ICDD# 01-089-2742), indicating high crystallinity. The absence of any Ni, NiS or NiO diffraction peaks in the doped Ni_2P indicates phase purity and successful incorporation of the dopants in Ni_2P crystal structure. In all the samples, diffraction from the (111) plane was found to be more intense indicative of the significant growth direction of the hexagonal Ni_2P. A closer examination of the most intense peak at $\approx 2\theta = 41$ (Fig. 1b) shows a slight shift to a lower angle for both increased Co and Fe-doping at the (111) plane of Ni_2P. This could be due to the substitution of Ni^{2+} ions by the larger Co^{2+} or Fe^{2+} ions, as supported by literature.[26,27]

The introduction of dopants could result in the modification of the electronic and optical properties of a material. The optical properties of the nanoparticles were therefore analyzed, and the spectra are shown in Fig. S2.† All the particles absorb photons within the UV–vis region of between 250 and 300 nm. The absorption peaks of the doped Ni_2P particles are slightly red-shifted relative to that of Ni_2P, which could be indicative of the Co and Fe dopants acting as auxochromes.

Scanning electron microscopy (SEM) images were used to observe the morphology of the synthesized nanoparticles. The SEM images reveal highly agglomerated spherically clustered compact particles that are well distributed, with the compactness of the nanoparticles decreasing as the Ni_2P nanoparticles are doped with Co and Fe (Fig. 2 and S3†). For a better insight into the morphology, transmission electron microscopy (TEM) was used, and the images are shown in Fig. S4.† The particles showed large irregular sheet-like morphology with smaller particles anchored/stacked on them. We also employed selected area electron diffraction (SAED) and high-resolution transmission electron microscopy (HRTEM) to further investigate the crystallinity and the micro-structure of as-synthesized dinickel phosphides (Fig. 2 and S4†). SAED images showed some well-defined spots indicative of crystallinity. However, the surface capping of catalysts with long alkyl chain surfactants may also result in reduced crystallinity to some extent. HRTEM images further confirmed the sheet-like morphology and crystallinity by showing clear lattice fringes that indexed well with the *d*-spacing from standard reference patterns for hexagonal Ni_2P.

The elemental composition of the prepared materials was undertaken to examine the composition of Ni_2P and the doped Ni_2P. The energy-dispersive X-ray spectroscopy (EDX) emissions of all prepared materials showed only Ni and P for Ni_2P and Co or Fe dopants for the doped Ni_2P, which is in agreement with the powder XRD. EDX elemental mapping of all the samples confirms the good distribution of the elements as well as the doping of Co and Fe into Ni_2P crystal lattice (Fig. 2). X-ray photoelectron spectroscopy (XPS) analyses of undoped Ni_2P and doped Ni_2P (Fe-Ni_2P and Co-Ni_2P) was performed since it can provide a direct evidence for the introduction of dopants that modulate the electronic structure of catalysts[28,29] and is given in Fig. 3 and S5.† The survey spectra of the Ni_2P, (Fe-Ni_2P and Co-Ni_2P) samples show the presence of Ni, P, O, C, (Fe and Co) elements as expected. The presence of oxygen and carbon in the
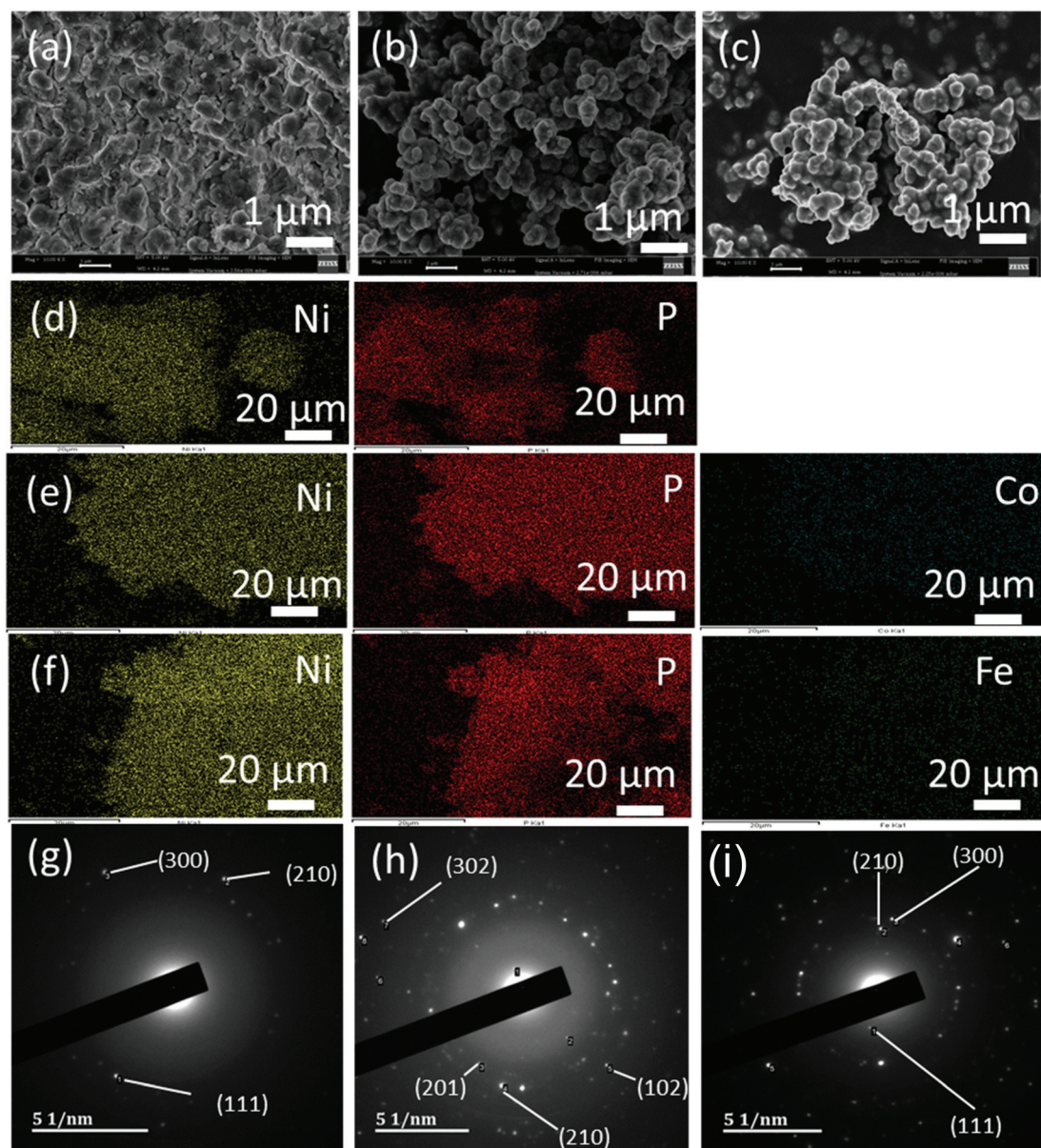
Fig. 2 SEM images of (a) Ni_2P (b) 10% $Co-Ni_2P$ and (c) 10% $Fe-Ni_2P$. Distribution of Ni, P and Co or Fe in (d) Ni_2P (e) 10% $Co-Ni_2P$ and (f) 10% $Fe-Ni_2P$. SAED of (g) Ni_2P (h) 10% $Co-Ni_2P$ and (i) 10% $Fe-Ni_2P$.

samples is attributed to surface oxidation[8] and adsorption.[30] Moreover the intense peak for carbon is due to the presence of capping agents on the surface of nanomaterials. Survey spectra analysis of these samples indicates the incorporation of Fe and Co in the doped Ni_2P which is in agreement with the p-XRD and SEM-EDX results. The XPS peak at 856.7 eV of the $Fe-Ni_2P$ is assigned to Ni^{2+} in the Ni $2p_{3/2}$ window while the satellite peak at 862.7 eV in the same window is attributed to surface oxidation (Fig. 3).[8] The peaks at 874.2, 875.9 and 880.4 eV are assigned to Ni of the $Fe-Ni_2P$ in the Ni $2p_{1/2}$ window. Similar results were observed for the Ni_2P and the $Co-Ni_2P$ samples as shown in Fig. S5.† The P 2p XPS regions (Fig. 3 and S5†) of these samples show peaks at 133, 134.6 and 130.9 eV for Ni_2P,

$Fe-Ni_2P$ and $Co-Ni_2P$ in the P $2p_{3/2}$ window, respectively, which are typical of the P of metal phosphides.[30] The $Co-Ni_2P$ material has another peak at 127.3 eV in the P $2p\frac{1}{2}$ window assigned to PO_x species which could be attributed to oxidation of the phosphorus in the sample.[30] High resolution spectra of the Fe 2p region of $Fe-Ni_2P$ (Fig. 3) indicated two peaks at 713 and 725.8 eV in the Fe $2p_{3/2}$ and Fe $2p_{1/2}$ windows, respectively, assigned to Fe^{3+}.[30] Similarly the Co 2p window of the XPS results of the $Co-Ni_2P$ show two peaks at 783.1 and 800.6 eV in the Co $2p_{3/2}$ and Co $2p_{1/2}$ windows, respectively, which may indicate presence of Co^{2+} and Co^{3+} as co-existing species.[28] These XPS results confirm surface capping of nanoparticles, surface oxidation and also show the successful doping of Fe and Co into Ni_2P.
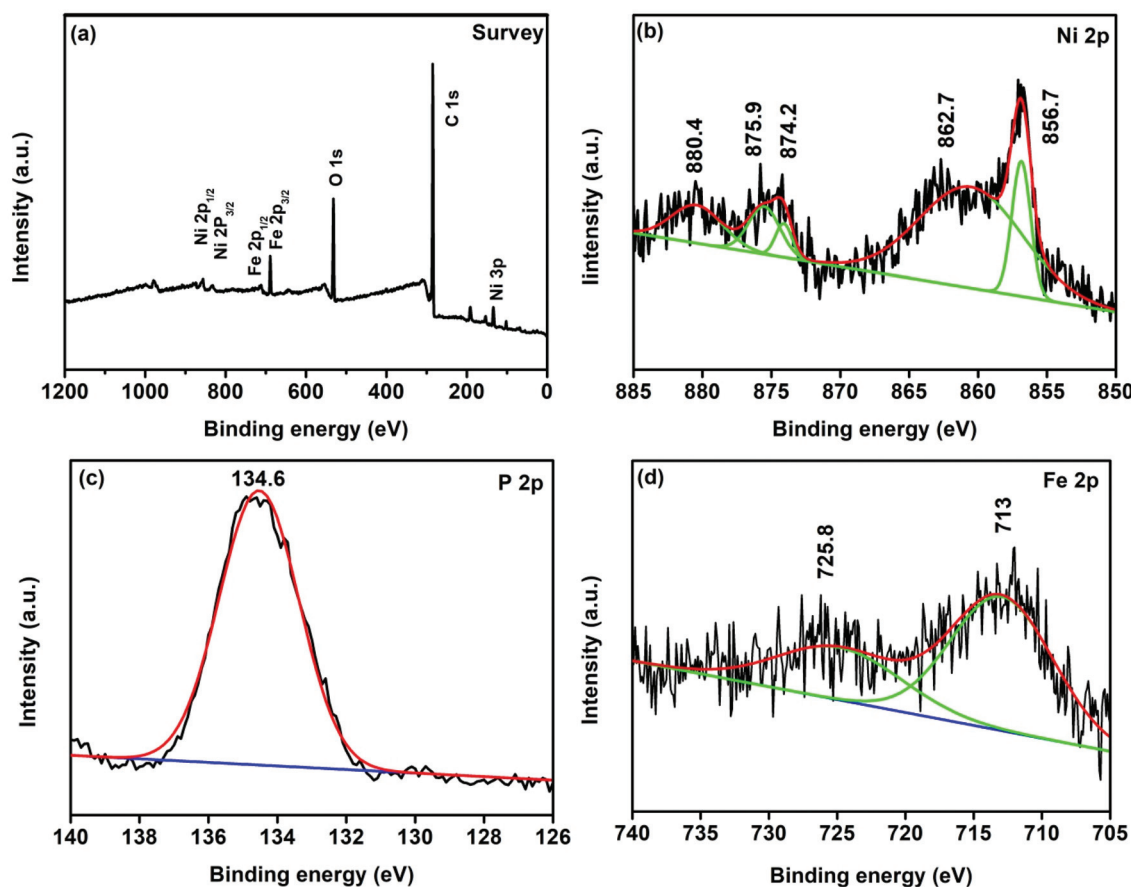
Fig. 3 XPS (a) survey spectrum of Fe-Ni$_2$P. (b) Ni 2p, (c) P 2p and (d) Fe 2p regions of Fe-Ni$_2$P.

Supercapacitance of Ni$_2$P and doped-Ni$_2$P electrodes

The potential of synthesized materials was studied for charge storage application and the analysis for Ni$_2$P, 10% Co-doped Ni$_2$P and 10% Fe-doped Ni$_2$P (henceforth referred to as Ni$_2$P, Co-Ni$_2$P and Fe-Ni$_2$P) are shown here, whereas, the results for 5% Co doped Ni$_2$P and 5% Fe doped Ni$_2$P are presented in the supplementary data. The charge storage capacities were investigated to determine the effect of doping on Ni$_2$P electrodes. The cyclic voltammetry (CV) and galvanostatic charge–discharge (GCD) measurements of the five electrodes (Ni$_2$P, Co-Ni$_2$P, Fe-Ni$_2$P, and 5% doped Co and 5% Fe doped Ni$_2$P) were obtained within the potential range of 0–0.6 (V, Hg/HgO) using 3 M KOH electrolyte. The CV test, which is the relationship between the current density and the electric potentials, of the electrodes for Ni$_2$P, Co-Ni$_2$P and Fe-Ni$_2$P electrodes is given in Fig. 4 whereas for 5% dopants *i.e.* 5% Co-Ni$_2$P and 5% Fe-Ni$_2$P are shown in Fig. S6,† at scan rates ranging from 2 mV s^{-1} to 300 mV s^{-1}. The CV plots for all the electrodes are indicative of the electrodes' pseudo-capacitive behavior.[31] The formation of these peaks could be due to surface faradaic reactions, as shown in eqn (1) and (2).[32,33]

$$Ni^{2+} + 2OH^- \rightarrow Ni(OH)_2 \tag{1}$$

$$Ni(OH)_2 + OH^- \rightarrow NiOOH + H_2O + e^- \tag{2}$$

We observed that the area under the CV curves of all the electrodes increases with an increase in scan rate, which is attributed to diffusion-limited kinetics.[31] Eqn (3) was employed to gain further insight into the diffusion-limited kinetics of the electrodes.[34]

$$i = av^b \tag{3}$$

In eqn (3), i is the peak current, v is the scan rate (mV s^{-1}), while a and b are variable parameters. The charge storage mechanism of electrodes can be separated by capacitive and diffusion-limited contributions. The charge storage mechanism of an electrode is therefore based on parameter b in eqn (3). The charge storage mechanism could be diffusion-limited when $b = 0.5$ or capacitive when $b = 1$. The b values of 0.51, 0.54, and 0.51 were obtained for Ni$_2$P, Co-Ni$_2$P, and Fe-Ni$_2$P electrodes, respectively, suggesting that diffusion-limited faradaic reaction dominates over the capacitive process in contribution to the charge storage capacity for all the electrodes (Fig. 5a). The dominance of diffusion-limited faradaic process suggests that the synthesized materials behave more like a battery, rather than the capacitance materials. To estimate the diffusion-controlled and capacitive contributions to the total energy storage of all the electrodes, a low and high
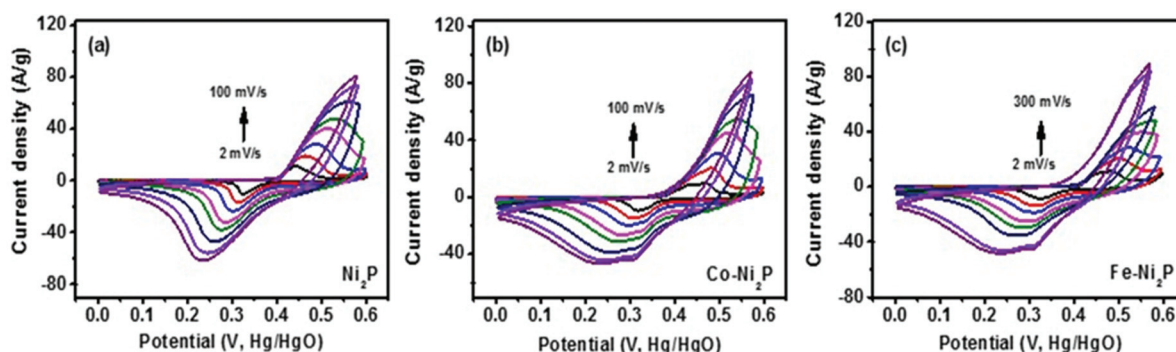
Fig. 4 CV curves of (a) Ni_2P, (b) $Co-Ni_2P$, and (c) $Fe-Ni_2P$ electrodes at various scan rates.
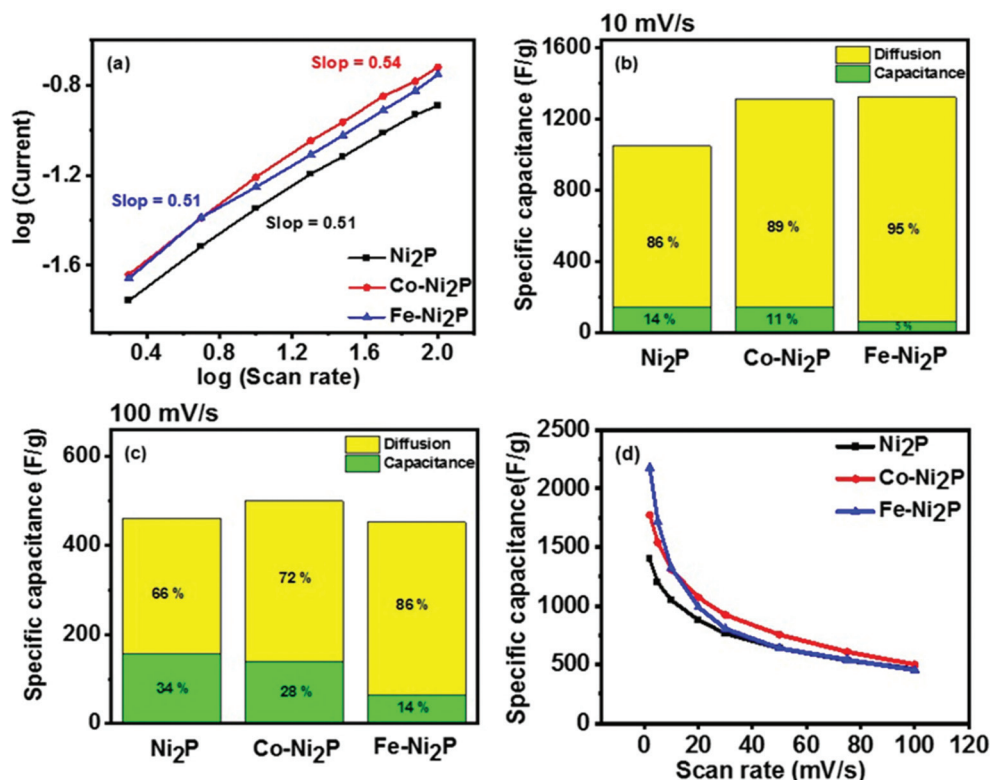

Fig. 5 (a) Log (current) *versus* log (scan rate) plot. (b) Capacitance and diffusion contributions at 10 mV s^{-1} scan rate and (c) at 100 mV s^{-1} scan rate. (d) Variation of specific capacitance as a function of scan rate for all samples.

scan rate of 10 and 100 mV s^{-1} was evaluated employing eqn (4),[34]

$$i = k_1\nu + k_2\nu^{1/2} \qquad (4)$$

where k_1 and k_2 are suitable values and $k_1\nu$ and $k_2\nu^{1/2}$ are capacitive and diffusion-limited contributions to total storage at a fixed potential, respectively. The total specific capacitance of an electrode is, therefore, a combination of the capacitive effect ($k_1\nu$) and the diffusion-controlled ($k_2\nu^{1/2}$) process. At 10 mV s^{-1} scan rate, the contribution of diffusion-limited ($k_2\nu^{1/2}$) process is 86, 89 and 95%, while that

of the capacitive process ($k_1\nu$) is 14, 11, 5% for Ni_2P, $Co-Ni_2P$ and $Fe-Ni_2P$, respectively (Fig. 5b). At a higher scan rate of 100 mV s^{-1}, the diffusion-limited contribution of 66, 72, 86% and the capacitive contribution of 34, 28 and 14% were observed for Ni_2P, $Co-Ni_2P$, $Fe-Ni_2P$, respectively (Fig. 5c). Fig. 5d gives the variation of specific capacitance as a function of the scan rate for Ni_2P, $Co-Ni_2P$ and $Fe-Ni_2P$ electrodes, which indicates excellent specific capacitance maintenance at different scan rates. These results suggest that the charge was mainly stored by a diffusion-controlled process for these electrodes, charge storage is maintained at higher scan rates, and
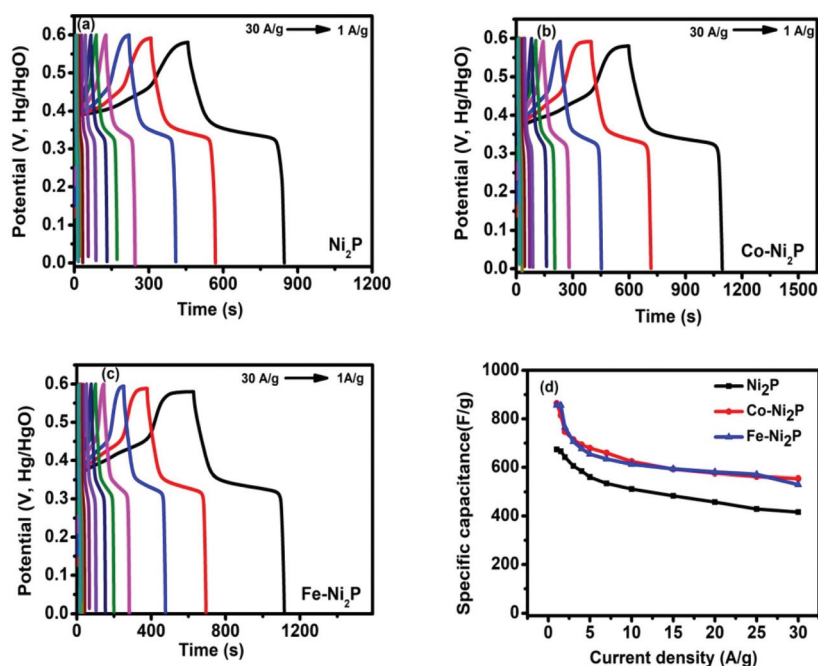
Fig. 6 GCD curves of (a) Ni$_2$P, (b) Co-Ni$_2$P, (c) Fe-Ni$_2$P electrodes at various current densities and (d) variation of specific capacitance as a function of current density.

that doping Ni$_2$P with Co or Fe synergistically improves the excellent storage capacity of the Ni$_2$P electrode.

Fig. 6a–c and S6† give the galvanostatic charge–discharge graphs of the five electrodes indicating the potential *vs.* time charge–discharge characteristics of the electrodes at different current densities. As shown in all the graphs, the plateau region was observed after a sharp potential drop. These plateau regions are attributed to the faradaic redox reactions, which corresponds to the CV results.[32] The Ni$_2$P, 5% Co-Ni$_2$P, and 5% Fe-Ni$_2$P electrodes recorded the specific capacitance of 674, 864, 856 F g^{-1} at 1A g^{-1} current density, respectively, based on the galvanostatic charge–discharge profiles. The recorded specific capacitance shows that doping Ni$_2$P with Co and Fe improves its supercapacitance properties. The superior performance of the Co-doped Ni$_2$P electrode compared to that of the Fe-doped Ni$_2$P electrode may be due to the superior theoretical specific capacitance of Co-based electrodes compared to that of Fe-based ones. Lu *et al.* employed an organic-phase strategy to synthesize Ni$_2$P electrodes that recorded a specific capacitance of 418 F, which is 40% lower than our Ni$_2$P electrode (674 F g^{-1}) at the same 1A g^{-1} current density.[33] The synthesized Ni$_2$P electrodes in that study were fabricated into a composite by coating with Ni, which improved their specific capacitance to 581 F g^{-1} compared to ours, where the doped Ni$_2$P electrodes had 864 F g^{-1} (Co-Ni$_2$P) and 856 F g^{-1} (Fe-Ni$_2$P), respectively. Liu *et al.* recently prepared a series of Ni$_2$P doped polypyrrole composites and tested their electrochemical application as supercapacitors.[35] Their 30% Ni$_2$P doped polypyrrole composite had the best performance of 476.5 F g^{-1}, which is 29% lower than our prepared Ni$_2$P (674 F

g^{-1}), 45% lower than Co-Ni$_2$P (864 F g^{-1}), and 44% lower than our Fe-Ni$_2$P (856 F g^{-1}) electrodes, respectively at 1A g^{-1} current density. A comparison of the supercapacitance of our electrodes to other similar nickel phosphide materials shows that our materials outperform other electrodes under similar conditions (Table S1†). The specific capacitance of an electrode generally decreases progressively with current density due to increasing limitation or infiltration of electrons and ions into the electrode surface. We, consequently, plotted the calculated specific capacitance values as a function of the current density, which is given in Fig. 6d and S6.† The specific capacitance of 417, 554, and 530 F g^{-1} was recorded for our Ni$_2$P, Co-Ni$_2$P, and Fe-Ni$_2$P electrodes at a high current density of 30 A g^{-1}. This result does not only indicate excellent stability of charge storage capacities for our electrodes but also shows that doping Ni$_2$P with Co and Fe improves the Ni$_2$P electrodes' charge retention capacity.

We also measured the long-term stability of the Ni$_2$P, Co-Ni$_2$P, and Fe-Ni$_2$P electrodes in 3000 charge–discharge cycles, as shown in Fig. 7. The electrodes showed a high retention capacity of 89, 85 and 74% of the initial cycles after 3000 cycles, along with 99% coulombic efficiency for Ni$_2$P, Co-Ni$_2$P and Fe-Ni$_2$P electrodes, respectively, suggesting good cyclic stability. The CV and GCD measurements show that doping our Ni$_2$P electrodes with Co and Fe dramatically improved its energy storage properties.

Water splitting of Ni$_2$P and TM doped-Ni$_2$P electrocatalysts

The electrocatalytic performance of Ni$_2$P, Co and Fe-doped materials for OER was measured in a standard 3 electrode
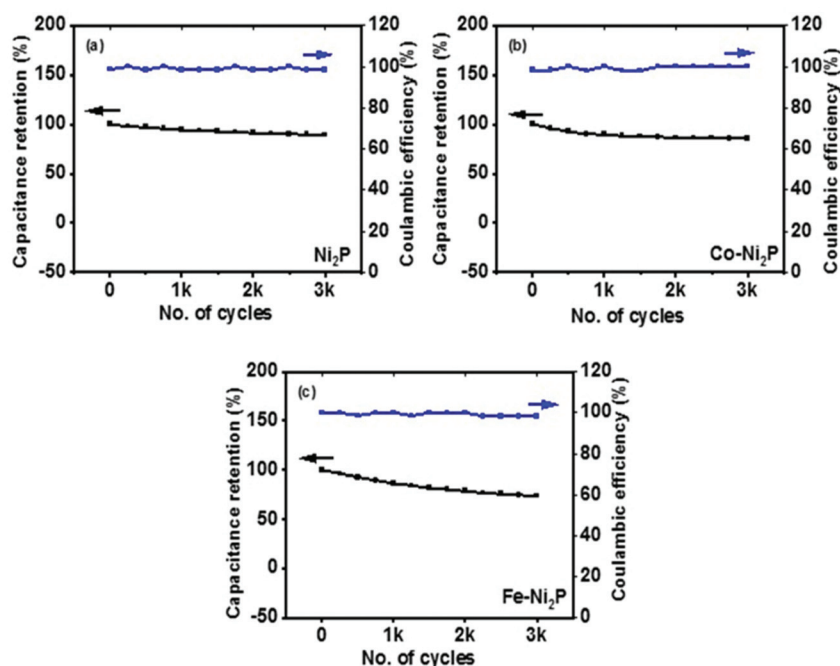
Fig. 7 Capacitance retention and coulombic efficiency of (a) Ni_2P, (b) $Co-Ni_2P$, (c) $Fe-Ni_2P$ for 3000 cycles.

system using 1M KOH electrolyte. Fig. 8a, b and S7† shows the OER polarization curve along with the Tafel slopes for Ni_2P, $Co-Ni_2P$ and $Fe-Ni_2P$ samples. The performance of an OER catalyst is evaluated conventionally by measuring the overpotential required to produce a current density of 10 mA cm^{-2}.[36] Our Ni_2P catalyst required an overpotential of 340 mV, while 320 and 259 mV was required for $Co-Ni_2P$ and $Fe-Ni_2P$ materials to deliver a current density of 10 mA cm^{-2}, respect-

ively. The 5% $Co-Ni_2P$ and 5% $Fe-Ni_2P$ electrodes required an overpotential of 298 and 355 mV, respectively to achieve the same current density. Furthermore, the Tafel slope of Ni_2P was measured as 103 mV dec^{-1}, but after Co and Fe doping, the slope of 98, 91, 130 and 80 mV dec^{-1} for 5% $Co-Ni_2P$, 10% $Co-Ni_2P$, 5% $Fe-Ni_2P$ and 10% $Fe-Ni_2P$, respectively was measured, suggesting faster reaction kinetics after Co and Fe doping.[37] It can be observed from these results that the higher concen-
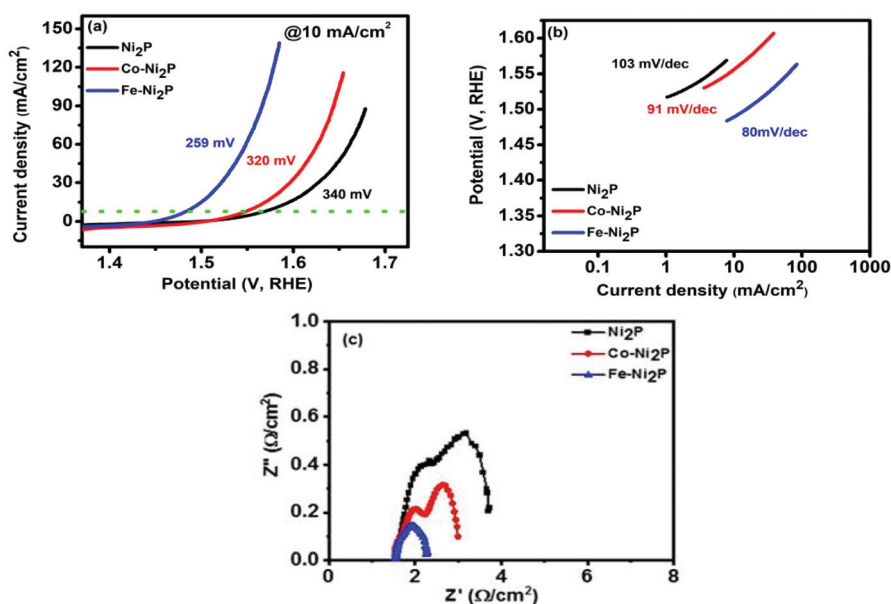

Fig. 8 (a) Polarization curves, (b) Tafel slopes of all samples for OER process, and (c) Nyquist plot at 0.6 V (V vs. SCE).

tration of iron *i.e.* 10% Fe-Ni$_2$P (259 mV) decreased the overpotential more as compared to all the samples. Density functional theory analysis has shown that doping the nickel phosphide system with Co leads to the substitution of the nickel metal with Co, which provides more active sites for OH$^-$ adsorption and subsequent OH$^-$ oxidation to form O$_2$.[13] The better performance of Fe-Ni$_2$P catalyst compared to Co-Ni$_2$P in OER could be due to better oxygen binding energy of Fe compared to Co in doped-Ni$_2$P catalyst. Fe-Ni$_2$P could therefore generate more moderately charged O anions to balance the binding energies among O*, HO* and HOO* species leading to lesser OER overpotential compared to Co-Ni$_2$P.[38] Lower Tafel slope values are associated with better OER catalysts, and it was observed that higher doping concentrations of Co and Fe into Ni$_2$P lowered the Tafel slopes significantly. It is interesting to note that, except 5% doped Fe-Ni$_2$P, all prepared catalysts had better Tafel slopes than that of the benchmark OER catalyst IrO$_2$ of 124.5 mV dec^{-1}. Doping a foreign atom into a crystal lattice can synergistically modulate its local coordination and electronic structure leading to improved OER activity.[39] The good performance of our Ni$_2$P electrode as an OER catalyst is further improved by doping, likely due the new environment created in it by incorporating Co and Fe into its crystal lattice.

Table S2† gives a further comparison of our electrodes as OER catalysts with respect to the OER activity of some state-of-the-art nickel phosphide-based electrocatalysts. The electrochemical impedance spectroscopy (EIS) measurements were employed to further study the effect of doping Co and Fe into the Ni$_2$P electrode. These measurements (Nyquist plots), which are typically used to explore the charge transfer processes at the electrode, were obtained within the frequency range of 0.05 Hz to 10 kHz with applied AC amplitude of 10 mV at 0.6 V (V *vs.* SCE) and are given in Fig. 8c and S7.† In the obtained Nyquist plots, two arcs are seen in Ni$_2$P, 5% Co-Ni$_2$P, Co-Ni$_2$P and 5% Fe-Ni$_2$P electrodes and only one semicircle was observed in the Fe-Ni$_2$P electrode. One arc at the high frequency represents the charge transfer resistance; the other arc at the low frequency represents the mass transfer resistance.[40] The diameter of the arc or semicircle is a function of the charge transfer resistance.[36] The smaller diameter of the arc at the high frequency for two of our electrodes indicates less charge transfer resistance and thus better charge transfer in the order Fe-Ni$_2$P > Co-Ni$_2$P > Ni$_2$P. The 5% Co-Ni$_2$P electrode had less charge transfer resistance compared to the 5% Fe-Ni$_2$P though both of them did not improve the charge transfer resistance of the Ni$_2$P electrode. In the case of arcs at low frequency, there is none for the Fe-Ni$_2$P graph but one in 5% Co-Ni$_2$P, Co-Ni$_2$P, 5% Fe-Ni$_2$P and Ni$_2$P graphs. The smaller diameter of the arc at low frequency for 5% Co-Ni$_2$P, Co-Ni$_2$P and 5% Fe-Ni$_2$P compared to Ni$_2$P indicate that these electrodes have less mass-transfer resistance than the Ni$_2$P electrode. These results of charge transfer resistance put
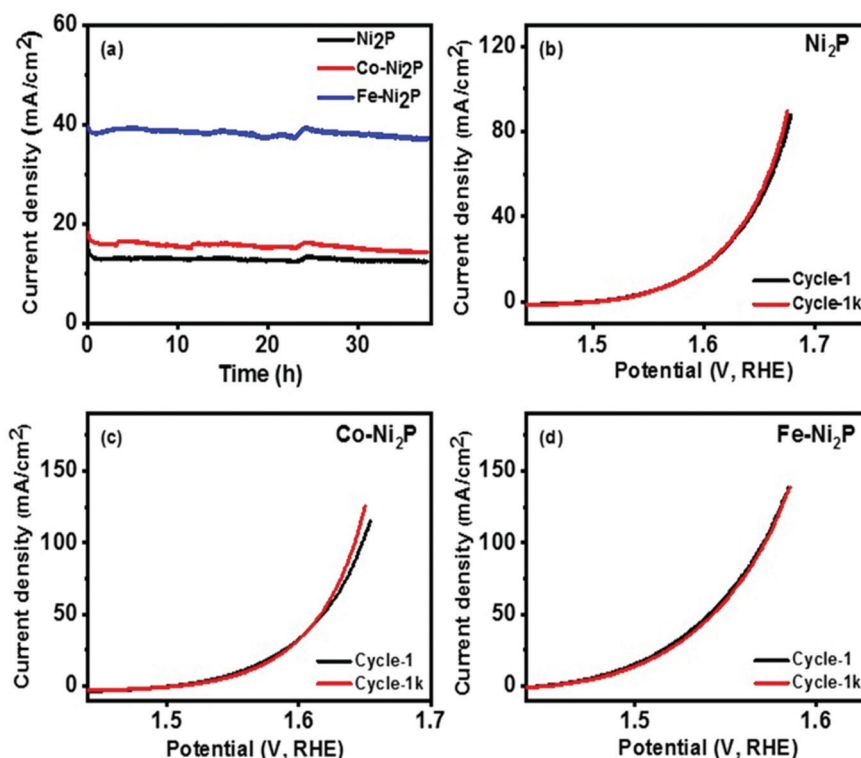

Fig. 9 (a) Chronoamperometry (CA) at 0.55 V (V *vs.* SCE) for all samples. OER polarization curves at different cycles for (b) Ni$_2$P, (c) Co-Ni$_2$P, and (d) Fe-Ni$_2$P.

together show that doping our Ni_2P with Co and Fe generally improves its OER electrocatalytic activity.

The long-term stability of a catalyst is crucial to its practical applications. The durability of our electrodes was therefore investigated employing the chronoamperometry (CA) test and polarization curve measurements, which are shown in Fig. 9a–d and S7.† CA measurements were done at 0.55 V (V vs. SCE), and a stable current density was delivered for all samples over 35 hours. A slight fluctuation was observed in the graphs for all samples during the CA test due to the bubbling caused by the occurrence of oxygen gas during oxygen evolution.[41] A measurement of the polarization curves for the 1st cycle and the 1000 cycles showed a negligible deviation between two curves for all the electrodes (Fig. 9b–d and S7†), indicating the excellent stability or durability of our electrodes as OER catalysts.

We also examined the electrocatalytic activity of our electrodes for hydrogen evolution reactions. Fig. 10 and S8† give the polarization curves and Tafel slopes of all the samples for the HER. The Ni_2P, 5% Co-Ni_2P, Co-Ni_2P, 5% Fe-Ni_2P and Fe-Ni_2P electrodes recorded an overpotential of 164, 156, 158, 68 and 202 mV to achieve a current density of 10 mA cm^{-2} with Tafel slopes of 117, 110, 113, 110 and 113 mV dec^{-1}, respectively. All the doped Ni_2P electrodes except Fe-Ni_2P decreased the overpotential of the un-doped Ni_2P electrode to attain 10 mA cm^{-2} current density for HER. The 5% Fe-Ni_2P electrode with 68 mV overpotential had the best synergistic catalytic performance with the un-doped Ni_2P electrode by reducing its overpotential by about 56%. All the doped electrodes had a lower calculated Tafel slope with respect to the un-doped Ni_2P electrode suggestive that doping in this study improved the reaction kinetics for HER. Doping Ni_2P with Co and Fe only improved slightly the catalytic and reaction kinetics of the Ni_2P electrode unlike the OER and supercapacitance. Kucernak et al. fabricated Ni_2P and $Ni_{12}P_5$ materials on glassy carbon electrodes and recorded about 270 and 450 mV overpotential with Tafel slopes of 84 and 108 mV dec^{-1}, which are lower than the performance of our electrodes.[42] Similarly, Tian et al. prepared $Ni_{12}P_5$ materials from a metal–organic framework that required about 670 mV overpotential to achieve 10 mA cm^{-2} current density with a Tafel slope of 270 mV dec^{-1}.[44] Our as prepared catalysts compare well or outperform other HER catalysts in electrocatalytic examinations and these comparative results are further shown in Table S3.†

The stability and durability of our electrodes for HER were also investigated and are shown in Fig. 11 and S8.† A comparison of the polarization curves for all the electrodes for 1000 cycles are well-matched, indicating excellent durability and stability.
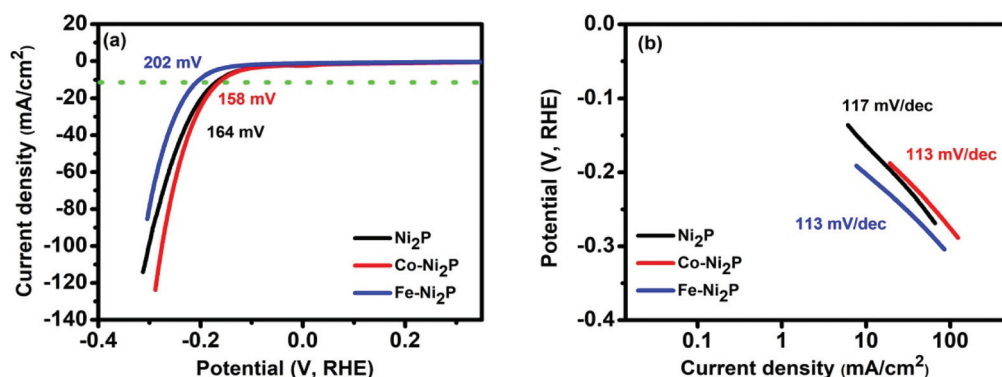

Fig. 10 (a) Polarization curves and (b) Tafel slopes of all samples for HER process.
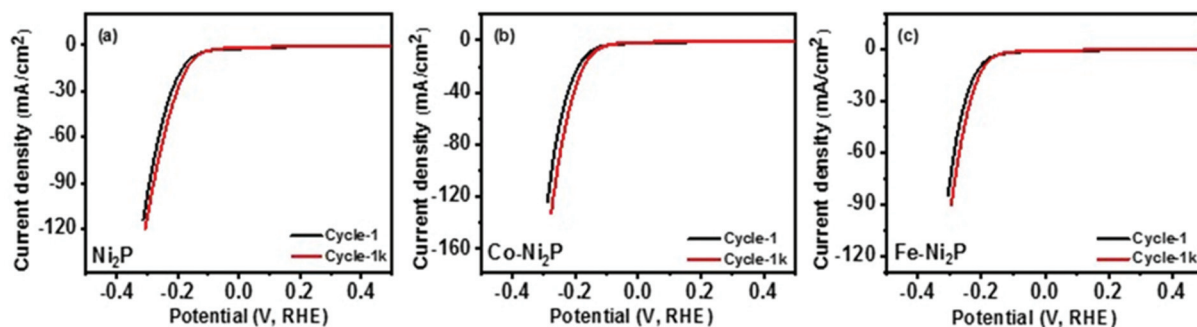

Fig. 11 HER Polarization curves at different cycles for (a) Ni_2P, (b) Co-Ni_2P, and (c) Fe-Ni_2P.

Conclusion

We have synthesized dithiophosphonate complexes of Ni, Co and Fe, and employed them to prepare Ni_2P, Co- and Fe-doped Ni_2P composites by the hot injection method. The doping of Co and Fe into Ni_2P did not change its crystal structure or introduce any impurity and were uniformly distributed. Doping was shown as a strategy to improve the electrochemical performance of the prepared Ni_2P with Co-Ni_2P, recording a supercapacitance of 864 F g^{-1} compared to Ni_2P with 674 F g^{-1} at 1A g^{-1} current density. Similarly, Fe-Ni_2P with an overpotential of 69 mV dec^{-1} to achieve a current density of 10 mA cm^{-2} enhanced the OER activity of Ni_2P that had an overpotential of 103 mV dec^{-1} to achieve the same current density. The prepared nickel phosphides also showed good catalytic activity in HER examinations and excellent stability as electrochemical catalysts, however, the doping did not significantly enhance the HER performance. These results indicate that our phosphide materials show good potential as a catalyst to be employed in water splitting and supercapacitor technologies.

Author contributions

Gwaza Eric Ayom: Performed the experimental work of synthesis of complexes and nanomaterials and their characterization, data analyses and curation, writing-original draft. Malik Dilshad Khan: Conceptualization, writing-review, writing-editing and validation. Jonghyun Choi: Performed electrocatalytic experiments and wrote the electrocatalysis part. Ram Krishna Gupta: Supervised the electrochemical experiments and reviewed the electrocatalysis write-up. Werner E. van Zyl: Supervised synthesis and characterization of complexes and writing-editing. Neerish Revaprasadu: Conceptualization, funding acquisition, supervision, writing-review and writing-editing.

Conflicts of interest

There are no conflicts to declare.

Acknowledgements

References

1 T. R. Cook, D. K. Dogutan, S. Y. Reece, Y. Surendranath, T. S. Teets and D. G. Nocera, *Chem. Rev.*, 2010, **110**, 6474–6502.

2 K. He, J. Zai, X. Liu, Y. Zhu, A. Iqbal, T. T. Tsega, Y. Zhang, N. Ali and X. Qian, *Appl. Catal., B*, 2020, **265**, 118594.

3 N. Liang, J. Zai, M. Xu, Q. Zhu, X. Wei and X. Qian, *J. Mater. Chem. A*, 2014, **2**, 4208–4216.

4 Y. Yan, T. Wang, X. Li, H. Pang and H. Xue, *Inorg. Chem. Front.*, 2017, **4**, 33–51.

5 G. E. Ayom, M. D. Khan, T. Ingsel, W. Lin, R. K. Gupta, S. J. Zamisa, W. E. van Zyl and N. Revaprasadu, *Chem. - Eur. J.*, 2020, **26**, 2693–2704.

6 H. M. El Sharkawy, D. M. Sayed, A. S. Dhmees, R. M. Aboushahba and N. K. Allam, *ACS Appl. Energy Mater.*, 2020, **3**, 9305–9314.

7 A. Ray, S. Sultana, L. Paramanik and K. M. Parida, *J. Mater. Chem. A*, 2020, **8**, 19196–19245.

8 G. E. Ayom, M. D. Khan, G. B. Shombe, J. Choi, R. K. Gupta, W. E. van Zyl and N. Revaprasadu, *Inorg. Chem.*, 2021, **60**, 11374–11384.

9 Z. Pu, T. Liu, I. S. Amiinu, R. Cheng, P. Wang, C. Zhang, P. Ji, W. Hu, J. Liu and S. Mu, *Adv. Funct. Mater.*, 2020, 2004009.

10 J. F. Callejas, C. G. Read, C. W. Roske, N. S. Lewis and R. E. Schaak, *Chem. Mater.*, 2016, **28**, 6017–6044.

11 K. He, T. Tadesse Tsega, X. Liu, J. Zai, X. H. Li, X. Liu, W. Li, N. Ali and X. Qian, *Angew. Chem., Int. Ed.*, 2019, **58**, 11903–11909.

12 B. Zhang, J. Zhang, X. Tang, Y. H. Lui and S. Hu, *Electrochim. Acta*, 2019, **294**, 297–303.

13 B. Qiu, L. Cai, Y. Wang, Z. Lin, Y. Zuo, M. Wang and Y. Chai, *Adv. Funct. Mater.*, 2018, **28**, 1706008.

14 Y. Li, J. Liu, C. Chen, X. Zhang and J. Chen, *ACS Appl. Mater. Interfaces*, 2017, **9**, 5982–5991.

15 Y. Liu, X. Zhang, K. Matras-Postolek and P. Yang, *J. Alloys Compd.*, 2020, **854**, 157111.

16 C. Lin, D. Wang, H. Jin, P. Wang, D. Chen, B. Liu and S. Mu, *J. Mater. Chem. A*, 2020, **8**, 4570–4578.

17 G. B. Shombe, M. D. Khan, A. M. Alenad, J. Choi, T. Ingsel, R. K. Gupta and N. Revaprasadu, *Sustainable Energy Fuels*, 2020, **4**, 5132–5143.

18 M. D. Khan, M. A. Malik and N. Revaprasadu, *Coord. Chem. Rev.*, 2019, **388**, 24–47.

19 W. Maneeprakorn, C. Q. Nguyen, M. A. Malik, P. O'Brien and J. Raftery, *Dalton Trans.*, 2009, 2103–2108.

20 C. M. Lukehart, S. B. Milne and S. R. Stock, *Chem. Mater.*, 1998, **10**, 903–908.

21 S. E. Habas, F. G. Baddour, D. A. Ruddy, C. P. Nash, J. Wang, M. Pan, J. E. Hensley and J. A. Schaidle, *Chem. Mater.*, 2015, **27**, 7580–7592.

22 Z. Liu, S. Yang, B. Sun, P. Yang, J. Zheng and X. Li, *Angew. Chem.*, 2020, **132**, 1991–1995.

23 J. Liu, M. Meyns, T. Zhang, J. Arbiol, A. Cabot and A. Shavel, *Chem. Mater.*, 2018, **30**, 1799–1807.

24 W. E. Van Zyl and J. P. Fackler, *Phosphorus, Sulfur Silicon Relat. Elem.*, 2000, **167**, 117–132.

25 W. E. van Zyl and J. D. Woollins, *Coord. Chem. Rev.*, 2013, **257**, 718–731.

26 K. Li, D. Rakov, W. Zhang and P. Xu, *Chem. Commun.*, 2017, **53**, 8199–8202.

27 J. Wang, X. Ma, F. Qu, A. M. Asiri and X. Sun, *Inorg. Chem.*, 2017, **56**, 1041–1044.

28 D. Ma, B. Hu, W. Wu, X. Liu, J. Zai, C. Shu, T. Tadesse Tsega, L. Chen, X. Qian and T. L. Liu, *Nat. Commun.*, 2019, **10**, 3367.

29 N. Liang, M. Wang, L. Jin, S. Huang, W. Chen, M. Xu, Q. He, J. Zai, N. Fang and X. Qian, *ACS Appl. Mater. Interfaces*, 2014, **6**, 11698–11705.

30 M. Li, J. Wang, X. Guo, J. Li, Y. Huang, S. Geng, Y. Yu, Y. Liu and W. Yang, *Appl. Surf. Sci.*, 2021, **536**, 147909.

31 D. Guragain, C. Zequine, R. Bhattarai, J. Choi, R. Gupta, X. Shen and S. Mishra, *MRS Adv.*, 2020, **5**, 2487–2494.

32 C. An, Y. Wang, Y. Wang, G. Liu, L. Li, F. Qiu, Y. Xu, L. Jiao and H. Yuan, *RSC Adv.*, 2013, **3**, 4628–4633.

33 Y. Lu, J.-k. Liu, X.-y. Liu, S. Huang, T.-q. Wang, X.-l. Wang, C.-d. Gu, J.-p. Tu and S. X. Mao, *CrystEngComm*, 2013, **15**, 7071–7079.

34 S. Bhoyate, P. K. Kahol, B. Sapkota, S. R. Mishra, F. Perez and R. K. Gupta, *Surf. Coat. Technol.*, 2018, **345**, 113–122.

35 S. Liu, Y. Chen, J. Ren, Y. Wang and W. Wei, *J. Solid State Electrochem.*, 2019, **23**, 3409–3418.

36 J. Kundu, S. Khilari, K. Bhunia and D. Pradhan, *Catal. Sci. Technol.*, 2019, **9**, 406–417.

37 N. R. Mucha, J. Som, J. Choi, S. Shaji, R. K. Gupta, H. M. Meyer, C. L. Cramer, A. M. Elliott and D. Kumar, *ACS Appl. Energy Mater.*, 2020, **3**, 8366–8374.

38 J. Song, C. Wei, Z.-F. Huang, C. Liu, L. Zeng, X. Wang and Z. J. Xu, *Chem. Soc. Rev.*, 2020, **49**, 2196–2214.

39 J. Jiang, F. Sun, S. Zhou, W. Hu, H. Zhang, J. Dong, Z. Jiang, J. Zhao, J. Li and W. Yan, *Nat. Commun.*, 2018, **9**, 1–12.

40 Q.-A. Huang, R. Hui, B. Wang and J. Zhang, *Electrochim. Acta*, 2007, **52**, 8144–8164.

41 I.-K. Ahn, W. Joo, J.-H. Lee, H. G. Kim, S.-Y. Lee, Y. Jung, J.-Y. Kim, G.-B. Lee, M. Kim and Y.-C. Joo, *Sci. Rep.*, 2019, **9**, 1–10.

42 A. R. Kucernak and V. N. N. Sundaram, *J. Mater. Chem. A*, 2014, **2**, 17435–17445.

43 B. Qiu, L. Cai, Y. Wang, Z. Lin, Y. Zuo, M. Wang and Y. Chai, Full paper, *Adv. Funct. Mater.*, 2018, **28**(17), 1706008–1706008.

44 T. Tian, L. Ai and J. Jiang, Metal–organic framework-derived nickel phosphides as efficient electrocatalysts toward sustainable hydrogen generation from water splitting, *RSC Adv.*, 2015, **5**, 10290–10295.